

Article

# Quantum-Sized Zinc Oxide Nanoparticles Synthesised within Mesoporous Silica (SBA-11) by Humid Thermal Decomposition of Zinc Acetate

Tariq Aqeel <sup>1,\*</sup> and Heather F. Greer <sup>2</sup> 

<sup>1</sup> Department of Science, College of Basic Education, The Public Authority of Applied Education and Training (PAAET) P.O. Box 23167, Safat 13092, Kuwait

<sup>2</sup> Department of Chemistry, University of Cambridge, Cambridge CB2 1EW, UK; hfg24@cam.ac.uk

\* Correspondence: tm.aqeel@paaet.edu.kw; Tel.: +965-222-1266 (ext. 6269)

Received: 10 June 2020; Accepted: 23 June 2020; Published: 26 June 2020



**Abstract:** A modified facile method is presented to synthesise quantum-sized zinc oxide nanoparticles within the pores of a mesoporous silica host (SBA-11). This method eliminates the 3 h alcohol reflux and the basic solution reaction steps of zinc acetate. The mesoporous structure and the ZnO nanoparticles were analysed by X-ray diffractometry, transmission electron microscopy, energy-dispersive X-ray spectroscopy, X-ray photoelectron spectroscopy, nitrogen sorption analysis and UV–VIS spectroscopy. These tests confirm the synthesis of ~1 nm sized ZnO within the pores of SBA-11 and that the porous structure remained intact after ZnO synthesis.

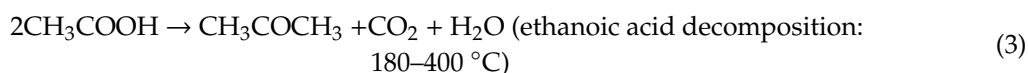
**Keywords:** quantum; ZnO; nanoparticles; SBA-11; XPS; UV–VIS; XRD

## 1. Introduction

Zinc oxide (ZnO) is a semiconductor material with a band gap of 3.37 eV [1]. It is widely used for its various properties, such as piezoelectric [2], optical [3], capacitors/supercapacitors [4,5], optical–electronic [6], solar [7], sensing [8,9], catalysis [10–12], optical catalysis [13], quantum size effect [14–16], antibacterial/antipathogens [17], and vaccine/tumour prevention [18,19]. Moreover, ZnO nanoparticles reactivity is inversely proportional to its size [20]. One of the methods of controlling the size of any nanoparticles, such as ZnO, is by confinement [21]. Introducing ZnO precursor into the pores of a mesoporous host [22] can prevent aggregation of the ZnO particles [23,24], stop them from leaching out as well as increase the surface area and activity of the particles. Moreover, having ZnO particles in the mesoporous silica host will introduce additional properties for both the guest/host materials and increase its implementation, for example in drug delivery, vaccination [18], photoluminescence [8,22], optical sensing, [25,26], photocatalysis [27], conversion of biomass [28], wound healing [29], hair follicle regeneration [30], tumour prevention [31–33], antibacterial effect [34] and antibiotic adsorption [35]. In addition, both materials silica and ZnO, are nontoxic and relatively cheap to produce [34].

On the other hand, there are many methods of converting zinc oxide precursor such as acetate ( $\text{Zn}(\text{CH}_3\text{CO}_2)_2 \cdot 2\text{H}_2\text{O}$ ), into ZnO; for example, by refluxing ( $\text{Zn}(\text{CH}_3\text{CO}_2)_2 \cdot 2\text{H}_2\text{O}$ ) in alcohol at 80 °C for 3 h and then reacting the product with a basic solution such as LiOH to form  $\text{Zn}(\text{OH})_x$  precursor [36] that would be dehydrated (to form metal oxide) to produce ZnO nanoparticles [37]. Meulenkamp's method [38] eliminates the 3 h reflux step; however both of these methods employed an alkaline solution for the hydrolysis of Zn acetate. The use of base tends to dissolve or destroy the porous arrangement of the silica host. Another method is Ariei et al.'s method [2], which is performed by the thermal decomposition of zinc acetate dihydrate powder under humid conditions. They reported that the thermal decomposition of zinc acetate dihydrate in a dry inert atmosphere tended to

sublimate the material at  $\sim 180$  °C, without forming ZnO. This sublimation stopped when a humid atmosphere is applied during thermal decomposition. Whereas, ZnO can be prepared by thermal decomposition of zinc acetate dihydrate under humid air at a temperature below 300 °C [2] according to the following steps:



Moreover, they found that the rate of forming ZnO is directly proportional to the water partial pressure [2].

Therefore, we created our own method by adapting different steps from these various mentioned methods to introduce ZnO nanoparticles into a mesoporous silica host. We removed the reflux step, which forms ZnO in the solution outside the host and terminated the basic hydrolysis reaction step to protect the mesoporous silica host from collapsing to produce quantum sized ZnO particles confined within the mesoporous silica. We used wet chemistry to dissolve zinc acetate dihydrate in ethanol by heating, then cooling the wet precursor to stop its aggregation [16,37], prior to introducing it to the host. We then applied Arii et al.'s method [2] of humid thermal decomposition of the confined precursor, inside the mesoporous host, to convert the precursor to ZnO nanoparticles, which is explained in detail in this paper.

## 2. Materials and Methods

### 2.1. Preparing SBA-11

SBA-11 was synthesised according to the method reported by Zhao et al. [39]. Simply, 4 g of polyoxyethylene (10) cetyl ether: [Brij 56:  $\text{C}_{16}\text{H}_{33}(\text{OCH}_2\text{CH}_2)_{10}\text{OH}$ ] was dissolved in an acidic water mixture of 20 g deionized  $\text{H}_2\text{O}$  + 80 g HCl (2M) by stirring at 40 °C. After dissolving the surfactant, it was cooled to room temperature (RT). Subsequently, 8.8 g of tetraethyl orthosilicate (TEOS) was added to the dissolved surfactant at RT and stirred slowly for 20 h. The product was then filtered, collected and washed several times with deionised water and left to air dry overnight at RT. Finally, the sample powder was calcined at 500 °C for 6 h at  $2 \text{ }^\circ\text{C min}^{-1}$ .

### 2.2. Synthesis of ZnO Particles inside SBA-11

First, 0.08 g of zinc acetate was dissolved in 20 mL methanol (MeOH) at 65 °C [38] under  $\text{N}_2$  cover for 30 min. Next, 1 g SBA-11 was heated at 160 °C for 2 h under  $\text{N}_2$  cover until dehydrated. The two substances were cooled to 0 °C [16], combined and stirred for 1 h. Stirring was stopped and the product was air dried overnight (16 h). The product was calcined at 220 °C under water bubbled air (humid air) for 30 min then under dry air at 500 °C for 4 h at  $3 \text{ }^\circ\text{C min}^{-1}$ . The powder was washed twice with MeOH to remove any external ZnO, indicated herein as ZnO-SBA-11. This produced 2.9 wt.% ZnO in SBA-11.

### 2.3. Control SBA-11

One gram of SBA-11 was heated at 160 °C for 2 h under  $\text{N}_2$  cover until dehydrated. The powder was cooled to 0 °C, then stirred for 1 h in 20 mL MeOH. Stirring was stopped and the product was air dried overnight (16 h). The product was calcined at 220 °C under water bubbled air (humid air) for 30 min then under dry air at 500 °C for 4 h at  $3 \text{ }^\circ\text{C min}^{-1}$  before it was washed twice with MeOH, indicated as control SBA-11.

All chemicals were purchased from Sigma-Aldrich (St. Louis, Missouri, USA) and used as received.

### 3. Results and Discussion

Figure 1a shows the low-angle powder X-ray diffraction (XRD) patterns of SBA-11 and ZnO-SBA-11. These patterns confirm that both samples are constructed of  $Pm3m$  cubic mesoporous arrangements [39], by the appearance of the main diffraction peaks (indicated with arrows). These peaks did not shift for ZnO-SBA-11 after the synthesis of ZnO inside the SBA-11 and after the second heat treatment associated with it, confirmed by extending an orange straight line through the (210) peak in both samples to intersect with the  $2\theta$  axis, at a single point of  $2.1^\circ$ . This indicates that the structure is stable and did not distort in the presence of ZnO particles. Moreover, the intensity decreased in some of the diffraction peaks, indicating that the ZnO formed in a preferred location. This can be determined by comparing the intensity difference between the (210) and (211) peaks in both samples. The differences are clarified by the aid of purple lines and arrows in Figure 1a with the top line representing the (210) maxima and the lower line indicating the (211) one. The height of h1 of SBA-11 is higher than h2 of ZnO-SBA-11. The wide-angle XRD patterns, Figure 1b, did not show any ZnO diffraction planes, which confirms that there are no ZnO particles on the outer surface of SBA-11 and the particles are likely inside the pores [8]. This may also indicate that the ZnO particles formed are too small to be distinguished from the background noise or to be detected by wide-angle XRD. Moreover, the broad XRD peak at the  $2\theta$  angles from 20 to 30, also confirms that the silica host (SBA-11) is non crystalline; amorphous walls surrounding an ordered porous arrangement.

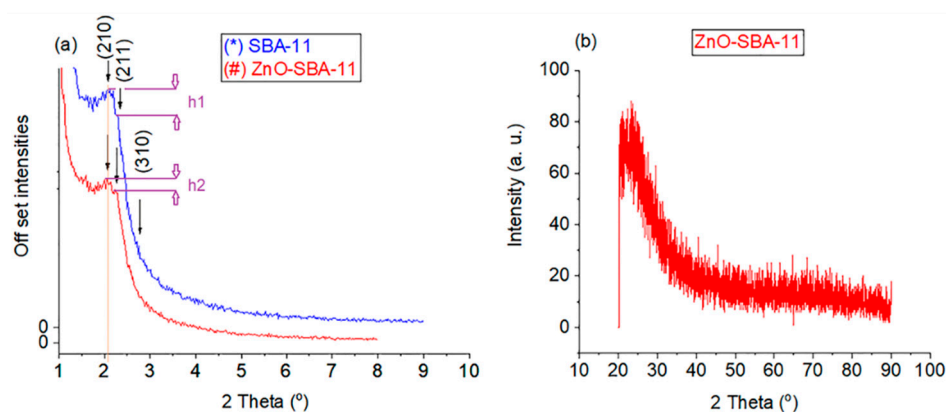


**Figure 1.** (a) Low-angle XRD patterns of (\*) SBA-11 and (#) ZnO-SBA-11, (b) wide-angle XRD pattern of ZnO-SBA-11.

Transmission electron microscopy (TEM) characterisation (Figure 2) was performed on the ZnO-SBA-11 sample to further analyse the structure after the incorporation of ZnO. Figure 2a–c is bright-field (BF) TEM images from different locations of the ZnO-SBA-11 sample, which confirm that the sample is porous. These pores extend throughout the entire particles (Figure 2a–c). The average pore diameter measured from these TEM images (Figure 2a–c and Figure S1) is 2 nm. Figure S1, a higher magnification image of Figure 2a clearly displays that some pore channels have sizes of 1.8 to 2.2 nm as indicated by the yellow lines. Bearing in mind that some of these pores are blocked by the top or bottom layers of the sample, because the electron beam can only penetrate through a few layers and projects the 3D structure into a 2D image. Depending on the view orientation, pore sizes might appear smaller than they actually are, especially for this cubic 3D structure at which the pores are interlocking. A more accurate pore size distribution is obtained from  $N_2$  sorption analysis. The darker spots in the BF image, some of which are indicated by red lines and circles in Figure 2b and Figure S1, might indicate the location of Zn atoms. Zn has a higher atomic weight than Si, so it will appear darker in the BF TEM images. Moreover, all BF TEM images show that these ZnO nanoparticles are attached to the internal walls of the pores, indicated by red lines and circles in Figure 2b and Figure S1. This probably occurred during the heat treatment, by losing the organic part of the precursor to form an interaction with the silica framework. This interaction is confirmed in the XPS section with ZnO-SBA-11 having

higher binding energy values than ZnO without a silica host. Furthermore, images Figure 2a,c reveal the long-range order of pores (parallel diagonal lines), whilst Figure 2b confirms the interconnected cubic arrangement nature of pores of ZnO-SBA-11, as confirmed by the XRD data (Figure 1). Figure 2d is the dark-field (DF) TEM image of Figure 2c, which indicates the existence of small ZnO particles and the absence of large aggregates of ZnO particles. Large ZnO particles would appear as bright spots in the DF TEM image. DF imaging is more sensitive to ZnO nanoparticles. This is because ZnO is crystalline and has a higher atomic number, whereas SBA-11 consists of amorphous silica with ordered interlocking pores. This is why SBA-11 appears dark in DF images, and only ZnO particles appears as bright spots. Moreover, we think that we have reached the resolution limits of this TEM instrument, especially in the DF mode, because the ZnO particles are very small. Figure 2e is the corresponding energy dispersive X-ray spectroscopy (EDX) spectra of ZnO-SBA-11 and Figure 2f is an enlargement of Figure 2e to show the relevant peaks clearly. The EDX spectra in Figure 2e,f confirm the composition constituents of ZnO-SBA-11, which are Si ( $K_{\alpha}$  peak at 1.74 keV and  $K_{\beta}$  peak at 1.84 keV), Zn ( $K_{\alpha}$  peak at 8.64 keV,  $K_{\beta}$  peak at 9.57 keV and  $L_{\alpha}$  peak at 1.01 keV) and O ( $K_{\alpha}$  peak at 0.52 keV), whereas Cu ( $K_{\alpha}$  peak at 8.05 keV,  $K_{\beta}$  peak at 8.90 keV and  $L_{\alpha}$  peak at 0.93 keV) is the support grid at which the sample was placed on during the TEM/EDX tests.

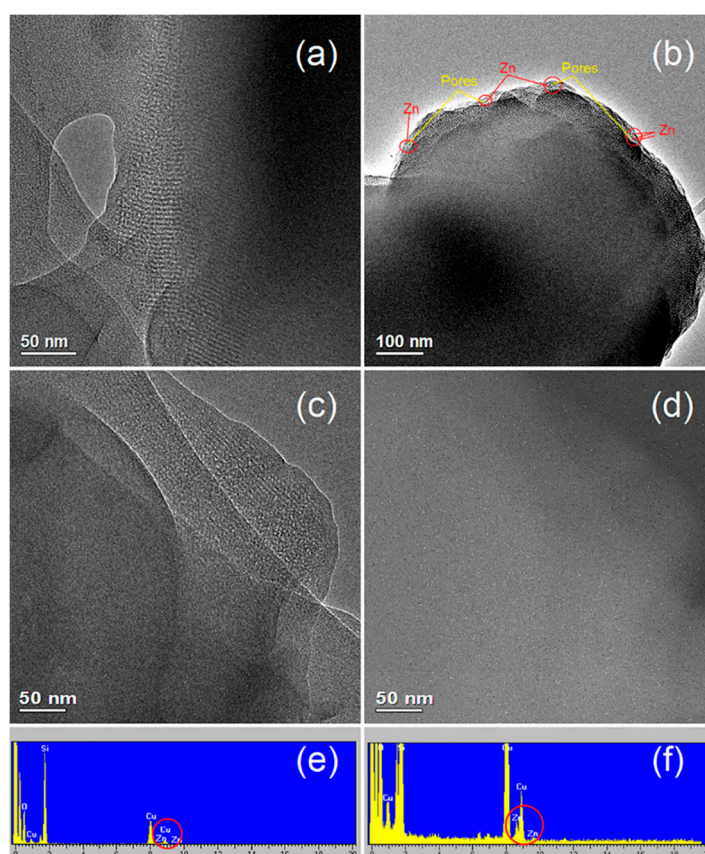


**Figure 2.** (a–c) Bright-field TEM images from different sections of ZnO-SBA-11, (d) is the dark-field TEM image of (c), (e) is the corresponding energy dispersive X-ray spectroscopy (EDX) of (c,d), and (f) is an enlargement of (e).

X-ray photoelectron spectroscopy (XPS) is conducted on both samples, SBA-11 and ZnO-SBA-11, to study the oxidation states of each constituent of the material's surface, subsurface and to confirm the syntheses of ZnO particles. Figure 3a,b represents the XPS main peak of Si at 103.5 eV that has been deconvoluted into two peaks at 103.2 and  $104 \pm 0.1$  eV, representing 2p orbital splitting into 2p<sub>3/2</sub> and 2p<sub>1/2</sub>, respectively [11,35]. These peaks are related to Si<sup>4+</sup> species in the SiO<sub>2</sub> structure.

Moreover, the oxygen XPS peak at  $532.9 \pm 0.2$  eV appeared in both samples and corresponds to  $O^{2-}$  in the  $SiO_2$  framework (Figure 3c,d) [11,35]. This peak was symmetrical for SBA-11 and asymmetrical for ZnO-SBA-11. This asymmetrical O peak in the latter contains an O peak at 531.5 eV. This peak corresponds to O in ZnO in the ZnO-SBA-11 matrix [11,40] and does not appear in SBA-11 (Figure 3d). Furthermore, two designated peaks appeared for the ZnO-SBA-11 sample, Figure 3e, at 1023 [12] and 1046 eV, as a result of 2p orbital splitting of  $Zn^{+2}$  of ZnO [11,34,41]. Moreover, the Zn 2p peaks are slightly higher by 1 eV than that of pure ZnO without a host, indicating that there is some Zn interaction with the Si atoms of the host [8]. This interaction occurs as a result of silicon being more electronegative than zinc, affecting Zn's electrons and securely maintaining ZnO particles in the pores. The difference between these two peaks is 23 eV [34]. Furthermore, by converting the atomic percentages (at. %) of the constituents to weight percentages (wt.%) from the XPS data, we calculated 2.4 wt.% ZnO in  $SiO_2$ . These calculations come very close to the experimental calculation that should produce 2.9 wt.% ZnO in  $SBA-11(SiO_2)$ . These results further confirm the formation ZnO in ZnO-SBA-11.

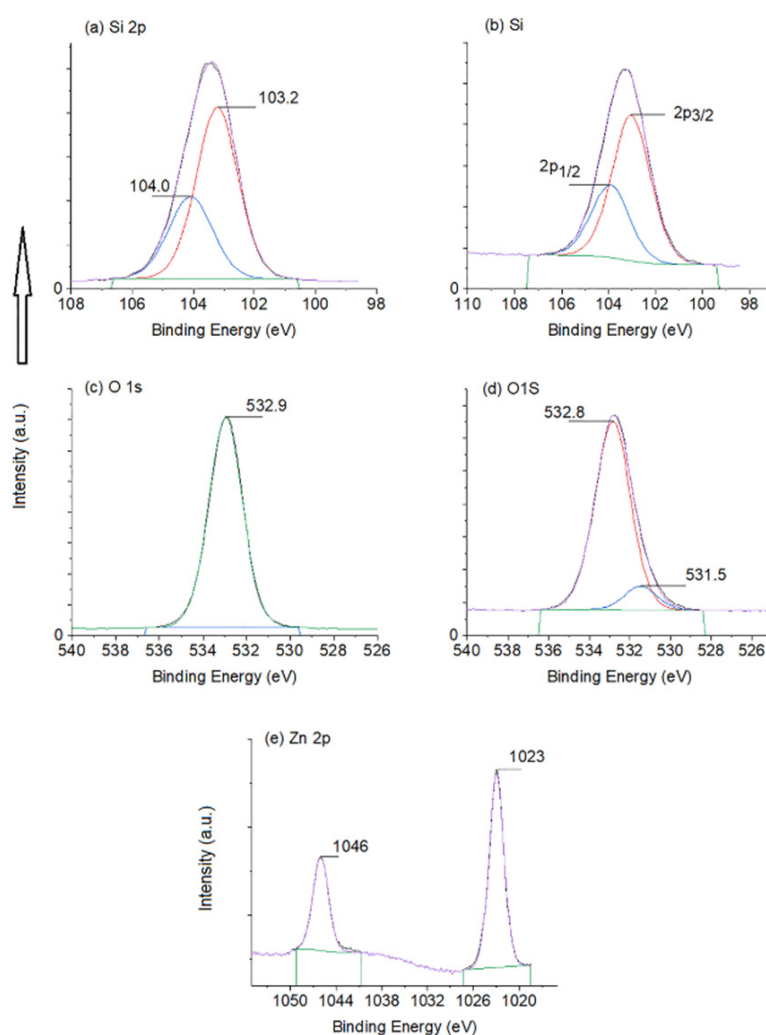


**Figure 3.** XPS of (a,c) SBA-11 and (b,d,e) ZnO-SBA-11.

$N_2$  sorption analysis was performed on SBA-11, ZnO-SBA-11 and a control SBA-11 sample to further study if changes occurred in the structure as a result of synthesising ZnO in SBA-11. The control sample is used to study in detail the effect of humid heat treatment on the structure. Heat treatment in the presence of water or steam is considered as an extreme condition that could destroy the mesoporous silica structure [42–44]. This control sample was prepared using a similar synthetic procedure as ZnO-SBA-11 but without the ZnO precursor. All samples produced similar isotherm

curves (Figure 4a–c). These isotherms are of “IVb type” typical of mesoporous materials, as classified by The International Union of Pure Applied Chemistry (IUPAC) report 2015 [45]. IVb isotherms are produced by mesoporous materials that possess pore diameters of less than 4 nm and the cycle is completely reversible (IUPAC report 2015), which is why IVb isotherms do not show any hysteresis curves. A 4 nm pore size is the minimum critical size to form condensates of liquid-like N<sub>2</sub> inside the pores. This formed condensate delays the liquid to vapor transition during the desorption cycle. Mismatch between the speed of forming condensates during adsorption and evaporation during desorption cycles produces hysteresis curves [45]. Moreover, these isotherms produced a saturation plateau after the point of inflection and pore condensation (at relative pressure of 0.3–0.9, Figure 4a,b). This indicates that the porous arrangements were intact (also confirmed by low-angle XRD and TEM). Furthermore, all samples produced a narrow pore size distribution between 2 and 3 nm (Figure 4d–f), having an average Barrett–Joyner–Halenda (BJH) pore size of  $2.15 \pm 0.05$  nm (similar to that obtained from TEM measurements). These pore sizes are in good agreement with the isotherm type and explains why the isotherms did not have hysteresis loops. In addition, the Brunauer–Emmett–Teller (BET) surface area of SBA-11 was  $815 \text{ m}^2 \text{ g}^{-1}$ , but after the humid heat treatment, it became  $666 \text{ m}^2 \text{ g}^{-1}$  for the control sample and after synthesising ZnO in it, it dropped to  $620 \text{ m}^2 \text{ g}^{-1}$  (ZnO-SBA-11). The difference in the surface areas between the control sample and the product (ZnO-SBA-11) is  $\sim 7\%$ , indicating the effect of having ZnO nanoparticles in the pores. The pore volumes were 0.44, 0.33 and  $0.32 \text{ cm}^3 \text{ g}^{-1}$ , respectively, a drop of  $\sim 25\%$  as a result of humid heat treatment and only  $\sim 3\%$  as a result of ZnO particles mainly occupying the pores (comparing the controlled sample to the final product). This 3–7% drop in pore volume or in surface area is an indication of synthesising ZnO nanoparticles within the pores. If these particles existed on the outer surfaces, they would increase the surface area of the product. We did not observe any significant changes in the pore sizes or any deformation of the structure between the control sample and product. There was a small shrinkage in the average pore sizes ( $\sim 0.05$  nm) between the starting SBA-11 and ZnO-SBA-11 product. The only differences observed between these samples were in the amount of N<sub>2</sub> volume absorbed by all the samples (Figure 4).

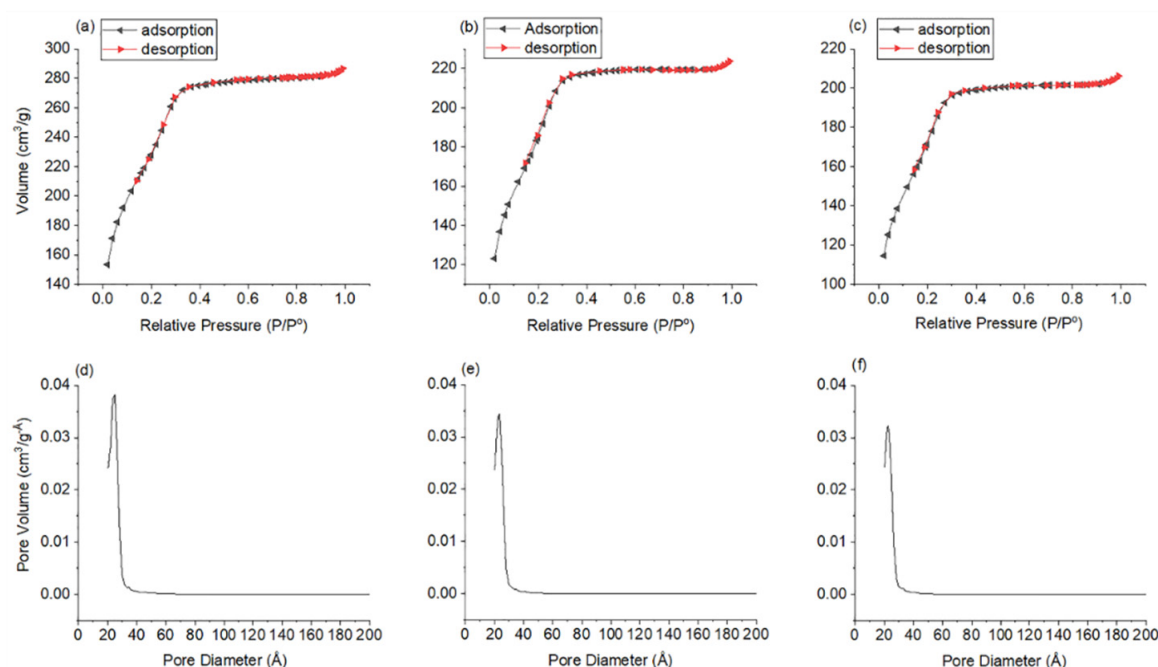


**Figure 4.** N<sub>2</sub> sorption analysis for (a,d) SBA-11, (b,e) control SBA-11 and (c,f) ZnO-SBA-11.

UV–VIS spectroscopy was conducted on ZnO-SBA-11 in the solid state to further confirm the formation of ZnO particles and to give an indication of their size (SBA-11 was used as a reference sample). The UV peak at 270 nm indicated by the arrow (Figure 5), confirms the existence of ZnO

nanoparticles [15,34] of size  $\sim 1$  nm [16,46]. It is known that as the size of ZnO particles decreases, the UV peak tends to move towards the blue wavelength region, known as a “blue-shift” as a result of quantum size effect [16,47]. This relatively sharp peak indicates a narrow size distribution of small ZnO particles in the sample. This could explain why we did not observe large bright spots in the dark-field TEM image (Figure 2d). Moreover, the significant drop in the spectra at 350 nm is the result of the bulb change in the instrument.

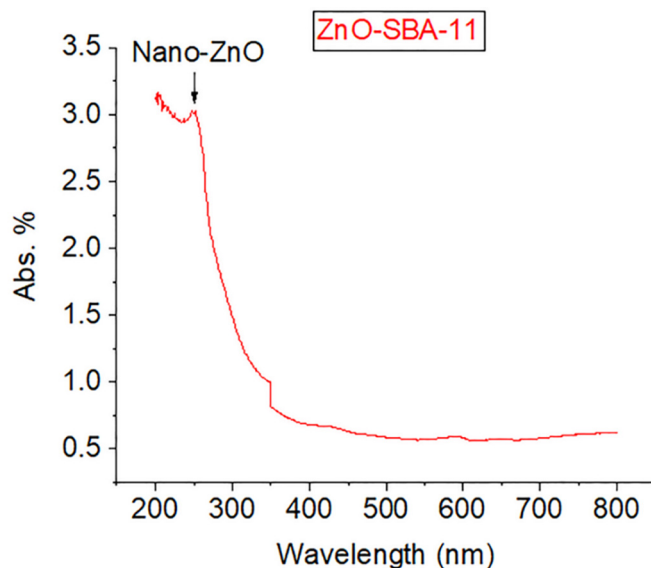


Figure 5. UV–VIS spectroscopy of ZnO-SBA-11 in the solid state.

All these characterisation methods confirm that zinc acetate dihydrate transformed into quantum-sized ZnO nanoparticles. These particles are imbedded in the internal walls of the SBA-11 pores and formed an interaction with the silica framework without disturbing the porous arrangements of the host. This will ensure that the particles do not leach out from the matrix during wet reactions and will not aggregate in larger groups. Moreover, these ZnO particles can be readily activated by UV sources, and the product could be employed in many applications and fields that have been presented in the Section 1, especially in wet or optical catalysis. Moreover, this simple ZnO synthesis method could be readily employed to other types of porous hosts and compositions.

#### 4. Conclusions

We present a facile method of preparing ZnO nanoparticles of small sizes,  $\sim 1$  nm, inside the internal walls of the SBA-11 pores without the use of basic exchange reagents or catalysts to convert zinc acetate to ZnO. Moreover, this method does not disturb the pore ordering or alter the mesoporous structure and maintains the high surface area and pore volume of the host material. This signifies that this material can be easily employed in wet, optical catalysis or adsorption reactions. In addition, this facile method could be applied for other porous structures and for different framework constituents.

**Supplementary Materials:** The following are available online at <http://www.mdpi.com/2073-4352/10/6/549/s1>, Figure S1. Bright-field TEM image of ZnO-SBA-11. A lower magnification image is shown in Figure 2a.

**Author Contributions:** T.A. performed the synthesis, XRD,  $N_2$  sorption, UV–VIS and wrote most of this manuscript. Conceptualization, T.A.; formal analysis, T.A.; funding acquisition, T.A.; investigation, T.A. and H.F.G.; methodology, T.A.; project administration, T.A.; resources, T.A.; supervision, T.A.; validation, T.A.; visualization, T.A.; writing—original draft, T.A.; writing—review and editing, T.A. and H.F.G.; H.F.G. performed the TEM/EDX microscopy and wrote the corresponding paragraph in addition to reviewing, editing and proofreading the whole manuscript. All authors have read and agreed to the published version of this manuscript.

**Funding:** This project was supported and funded by the Public Authority of Applied Education and Training (PAAET: Project No. BE-15-04 titled “Using Mesoporous Materials to Absorb Sulphur Compounds from Kuwaiti Petroleum Products”).

**Acknowledgments:** This project is performed in collaboration with Duncan Bruce at the University of York (N<sub>2</sub> sorption and XRD experiments) and Ali Bumajdad and the support of the research administration at Kuwait University by providing the XPS (Project No. GS01/05) and UV-VIS instruments (No. GS01/10) are acknowledged.

**Conflicts of Interest:** The authors declare that there is no conflict of interest.

## References

1. Munirah; Khan, Z.R.; Aziz, A.; Khan, M.S.; Khandaker, M.U. Influence of zinc concentration on band gap and sub-band gap absorption on ZnO nanocrystalline thin films sol-gel grown. *Mater. Sci. Pol.* **2017**, *35*, 246–253. [[CrossRef](#)]
2. Arii, T.; Kishi, A. The effect of humidity on thermal process of zinc acetate. *Thermochim. Acta* **2003**, *400*, 175–185. [[CrossRef](#)]
3. Schmitt, M. Synthesis and testing of ZnO nanoparticles for photo-initiation: Experimental observation of two different non-migration initiators for bulk polymerization. *Nanoscale* **2015**, *7*, 9532–9544. [[CrossRef](#)] [[PubMed](#)]
4. Yu, M.; Qiu, W.; Wang, F.; Zhai, T.; Fang, P.; Lu, X.; Tong, Y. Three dimensional architectures: Design, assembly and application in electrochemical capacitors. *J. Mater. Chem. A* **2015**, *3*, 15792–15823. [[CrossRef](#)]
5. Zhang, G.; Xiao, X.; Li, B.; Gu, P.; Xue, H.; Pang, H. Transition metal oxides with one-dimensional/one-dimensional-analogue nanostructures for advanced supercapacitors. *J. Mater. Chem. A* **2017**, *5*, 8155–8186. [[CrossRef](#)]
6. Hosono, E.; Fujihara, S.; Kimura, T. Synthesis, structure and photoelectrochemical performance of micro/nano-textured ZnO/eosin Y electrodes. *Electrochim. Acta* **2004**, *49*, 2287–2293. [[CrossRef](#)]
7. Stroyuk, O.; Raevskaya, A.; Gaponik, N. Solar light harvesting with multinary metal chalcogenide nanocrystals. *Chem. Soc. Rev.* **2018**, *47*, 5354–5422. [[CrossRef](#)]
8. Jiang, Q.; Wu, Z.Y.; Wang, Y.M.; Cao, Y.; Zhou, C.F.; Zhu, J.H. Fabrication of photoluminescent ZnO/SBA-15 through directly dispersing zinc nitrate into the as-prepared mesoporous silica occluded with template. *J. Mater. Chem.* **2006**, *16*, 1536–1542. [[CrossRef](#)]
9. Li, Z.; Li, H.; Wu, Z.; Wang, M.; Luo, J.; Torun, H.; Hu, P.; Yang, C.; Grundmann, M.; Liu, X.; et al. Advances in designs and mechanisms of semiconducting metal oxide nanostructures for high-precision gas sensors operated at room temperature. *Mater. Horizons* **2019**, *6*, 470–506. [[CrossRef](#)]
10. Zhong, J.; Yang, X.; Wu, Z.; Liang, B.; Huang, Y.; Zhang, T. State of the art and perspectives in heterogeneous catalysis of CO<sub>2</sub> hydrogenation to methanol. *Chem. Soc. Rev.* **2020**, *49*, 1385–1413. [[CrossRef](#)] [[PubMed](#)]
11. Liu, Y.; Shen, J.; Zhao, L.; Wang, W.; Gong, W.; Zheng, F. Zinc-iron silicate for heterogeneous catalytic ozonation of acrylic acid: Efficiency and mechanism. *RSC Adv.* **2020**, *10*, 9146–9154. [[CrossRef](#)]
12. Doghri, H.; Baranova, E.A.; Albela, B.; Saïd-Zina, M.; Bonneviot, L. A bio-inspired zinc finger analogue anchored in 2D hexagonal mesoporous silica for room temperature CO<sub>2</sub> activation: Via a hydrogenocarbonate route. *New J. Chem.* **2017**, *41*, 6795–6809. [[CrossRef](#)]
13. Marković, S.; Stojković Simatović, I.; Ahmetović, S.; Veselinović, L.; Stojadinović, S.; Rac, V.; Škapin, S.D.; Bajuk Bogdanović, D.; Janković Častvan, I.; Uskoković, D. Surfactant-assisted microwave processing of ZnO particles: A simple way for designing the surface-to-bulk defect ratio and improving photo(electro)catalytic properties. *RSC Adv.* **2019**, *9*, 17165–17178. [[CrossRef](#)]
14. Du, Z.; Artemyev, M.; Wang, J.; Tang, J. Performance improvement strategies for quantum dot-sensitized solar cells: A review. *J. Mater. Chem. A* **2019**, *7*, 2464–2489. [[CrossRef](#)]
15. Tokumoto, M.S.; Briois, V.; Santilli, C.V.; Pulcinelli, S.H. Preparation of ZnO Nanoparticles: Structural Study. *J. Sol-Gel Sci. Technol.* **2003**, *26*, 547–551. [[CrossRef](#)]
16. Segets, D.; Gradl, J.; Taylor, R.K.; Vassilev, V.; Peukert, W. Analysis of optical absorbance spectra for the determination of ZnO nanoparticle size distribution, solubility, and surface energy. *ACS Nano* **2009**, *3*, 1703–1710. [[CrossRef](#)] [[PubMed](#)]

17. Mahamuni, P.P.; Patil, P.M.; Dhanavade, M.J.; Badiger, M.V.; Shadija, P.G.; Lokhande, A.C.; Bohara, R.A. Synthesis and characterization of zinc oxide nanoparticles by using polyol chemistry for their antimicrobial and antibiofilm activity. *Biochem. Biophys. Rep.* **2019**, *17*, 71–80. [[CrossRef](#)]
18. Li, X.; Wang, X.; Ito, A. Tailoring inorganic nanoadjuvants towards next-generation vaccines. *Chem. Soc. Rev.* **2018**, *47*, 4954–4980. [[CrossRef](#)]
19. Cai, Q.; Xu, J.; Yang, D.; Dai, Y.; Yang, G.; Zhong, C.; Gai, S.; He, F.; Yang, P. Polypyrrole-coated UCNPs@mSiO<sub>2</sub>@ZnO nanocomposite for combined photodynamic and photothermal therapy. *J. Mater. Chem. B* **2018**, *6*, 8148–8162. [[CrossRef](#)]
20. Ramakrishna, G.; Ghosh, H.N. Effect of particle size on the reactivity of quantum size ZnO nanoparticles and charge-transfer dynamics with adsorbed catechols. *Langmuir* **2003**, *19*, 3006–3012. [[CrossRef](#)]
21. Aqeel, T.; Bumajdad, A. facile and direct preparation of ultrastable mesoporous silica with silver nanoclusters: High surface area. *ChemistryOpen* **2020**, *9*, 87–92. [[CrossRef](#)] [[PubMed](#)]
22. Raevskaya, A.E.; Panasiuk, Y.V.; Stroyuk, O.L.; Kuchmiy, S.Y.; Dzhan, V.M.; Milekhin, A.G.; Yeryukov, N.A.; Sveshnikova, L.A.; Rodyakina, E.E.; Plyusnin, V.F.; et al. Spectral and luminescent properties of ZnO-SiO<sub>2</sub> core-shell nanoparticles with size-selected ZnO cores. *RSC Adv.* **2014**, *4*, 63393–63401. [[CrossRef](#)]
23. Tokumoto, M.S.; Pulcinelli, S.H.; Santilli, C.V.; Craievich, A.F. SAXS study of the kinetics of formation of ZnO colloidal suspensions. *J. Non. Cryst. Solids* **1999**, *247*, 176–182. [[CrossRef](#)]
24. Mikrajuddin; Iskandar, F.; Okuyama, K.; Shi, F.G. Stable photoluminescence of zinc oxide quantum dots in silica nanoparticles matrix prepared by the combined sol-gel and spray drying method. *J. Appl. Phys.* **2001**, *89*, 6431–6434. [[CrossRef](#)]
25. Zhou, Z.; Lu, K.; Wei, X.; Hao, T.; Xu, Y.; Lv, X.; Zhang, Y. A mesoporous fluorescent sensor based on ZnO nanorods for the fluorescent detection and selective recognition of tetracycline. *RSC Adv.* **2016**, *6*, 71061–71069. [[CrossRef](#)]
26. He, J.H.; Ho, S.T.; Wu, T.B.; Chen, L.J.; Wang, Z.L. Electrical and photoelectrical performances of nano-photodiode based on ZnO nanowires. *Chem. Phys. Lett.* **2007**, *435*, 119–122. [[CrossRef](#)]
27. Zhou, K.; Ding, Y.; Zhang, L.; Wu, H.; Guo, J. Synthesis of mesoporous ZnO/TiO<sub>2</sub>-SiO<sub>2</sub> composite material and its application in photocatalytic adsorption desulfurization without the addition of an extra oxidant. *Dalt. Trans.* **2020**, *49*, 1600–1612. [[CrossRef](#)]
28. Sudarsanam, P.; Peeters, E.; Makshina, E.V.; Parvulescu, V.I.; Sels, B.F. Advances in porous and nanoscale catalysts for viable biomass conversion. *Chem. Soc. Rev.* **2019**, *48*, 2366–2421. [[CrossRef](#)]
29. Nethi, S.K.; Das, S.; Patra, C.R.; Mukherjee, S. Recent advances in inorganic nanomaterials for wound-healing applications. *Biomater. Sci.* **2019**, *7*, 2652–2674. [[CrossRef](#)]
30. Zhang, Y.; Chang, M.; Bao, F.; Xing, M.; Wang, E.; Xu, Q.; Huan, Z.; Guo, F.; Chang, J. Multifunctional Zn doped hollow mesoporous silica/polycaprolactone electrospun membranes with enhanced hair follicle regeneration and antibacterial activity for wound healing. *Nanoscale* **2019**, *11*, 6315–6333. [[CrossRef](#)]
31. Qian, G.; Wang, X.; Li, X.; Ito, A.; Sogo, Y.; Ye, J. An immuno-potentiating vehicle made of mesoporous silica-zinc oxide micro-rosettes with enhanced doxorubicin loading for combined chemoimmunotherapy. *Chem. Commun.* **2019**, *55*, 961–964. [[CrossRef](#)] [[PubMed](#)]
32. Wen, J.; Yang, K.; Liu, F.; Li, H.; Xu, Y.; Sun, S. Diverse gatekeepers for mesoporous silica nanoparticle based drug delivery systems. *Chem. Soc. Rev.* **2017**, *46*, 6024–6045. [[CrossRef](#)]
33. Wu, S.; Huang, X.; Du, X. pH- and redox-triggered synergistic controlled release of a ZnO-gated hollow mesoporous silica drug delivery system. *J. Mater. Chem. B* **2015**, *3*, 1426–1432. [[CrossRef](#)] [[PubMed](#)]
34. Qiu, S.; Zhou, H.; Shen, Z.; Hao, L.; Chen, H.; Zhou, X. Synthesis, characterization, and comparison of antibacterial effects and elucidating the mechanism of ZnO, CuO and CuZnO nanoparticles supported on mesoporous silica SBA-3. *RSC Adv.* **2020**, *10*, 2767–2785. [[CrossRef](#)]
35. Huang, D.; Zhang, Y.; Zhang, J.; Wang, H.; Wang, M.; Wu, C.; Cheng, D.; Chi, Y.; Zhao, Z. The synergetic effect of a structure-engineered mesoporous SiO<sub>2</sub>-ZnO composite for doxycycline adsorption. *RSC Adv.* **2019**, *9*, 38772–38782. [[CrossRef](#)]
36. Govender, K.; Boyle, D.S.; Kenway, P.B.; O'Brien, P. Understanding the factors that govern the deposition and morphology of thin films of ZnO from aqueous solution. *J. Mater. Chem.* **2004**, *14*, 2575–2591. [[CrossRef](#)]
37. Spanhel, L.; Anderson, M.A. Semiconductor clusters in the sol-gel process: Quantized aggregation, gelation, and crystal growth in concentrated ZnO colloids. *J. Am. Chem. Soc.* **1991**, *113*, 2826–2833. [[CrossRef](#)]
38. Meulenkaamp, E.A. Synthesis and growth of ZnO nanowires. *J. Phys. Chem. B* **1998**, *102*, 5566–5572. [[CrossRef](#)]

39. Zhao, D.; Huo, Q.; Feng, J.; Chmelka, B.F.; Stucky, G.D. Nonionic triblock and star diblock copolymer and oligomeric surfactant syntheses of highly ordered, hydrothermally stable, mesoporous silica structures. *J. Am. Chem. Soc.* **1998**, *120*, 6024–6036. [[CrossRef](#)]
40. Wei, X.Q.; Man, B.Y.; Liu, M.; Xue, C.S.; Zhuang, H.Z.; Yang, C. Blue luminescent centers and microstructural evaluation by XPS and Raman in ZnO thin films annealed in vacuum, N<sub>2</sub> and O<sub>2</sub>. *Phys. B Condens. Matter* **2007**, *388*, 145–152. [[CrossRef](#)]
41. Tkachenko, O.P.; Klementiev, K.V.; Löffler, E.; Ritzkopf, I.; Schüth, F.; Bandyopadhyay, M.; Grabowski, S.; Gies, H.; Hagen, V.; Muhler, M.; et al. The structure of zinc and copper oxide species hosted in porous siliceous matrices. *Phys. Chem. Chem. Phys.* **2003**, *5*, 4325–4334. [[CrossRef](#)]
42. Mokaya, R. Improving the stability of mesoporous MCM-41 silica via thicker more highly condensed pore walls. *J. Phys. Chem. B* **1999**, *103*, 10204–10208. [[CrossRef](#)]
43. Cassiers, K.; Linssen, T.; Mathieu, M.; Benjelloun, M.; Schrijnemakers, K.; Van Der Voort, P.; Cool, P.; Vansant, E.F. A detailed study of thermal, hydrothermal, and mechanical stabilities of a wide range of surfactant assembled mesoporous silicas. *Chem. Mater.* **2002**, *14*, 2317–2324. [[CrossRef](#)]
44. Linssen, T.; Cassiers, K.; Cool, P.; Vansant, E.F. Mesoporous templated silicates: An overview of their synthesis, catalytic activation and evaluation of the stability. *Adv. Colloid Interface Sci.* **2003**, *103*, 121–147. [[CrossRef](#)]
45. Thommes, M.; Kaneko, K.; Neimark, A.V.; Olivier, J.P.; Rodriguez-Reinoso, F.; Rouquerol, J.; Sing, K.S.W. Physisorption of gases, with special reference to the evaluation of surface area and pore size distribution (IUPAC Technical Report). *Pure Appl. Chem.* **2015**, *87*, 1051–1069. [[CrossRef](#)]
46. Zhang, W.H.; Shi, J.L.; Wang, L.Z.; Yan, D.S. Preparation and characterization of ZnO clusters inside mesoporous silica. *Chem. Mater.* **2000**, *12*, 1408–1413. [[CrossRef](#)]
47. Pesika, N.S.; Stebe, K.J.; Searson, P.C. Relationship between absorbance spectra and particle size distributions for quantum-sized nanocrystals. *J. Phys. Chem. B* **2003**, *107*, 10412–10415. [[CrossRef](#)]



© 2020 by the authors. Licensee MDPI, Basel, Switzerland. This article is an open access article distributed under the terms and conditions of the Creative Commons Attribution (CC BY) license (<http://creativecommons.org/licenses/by/4.0/>).